70 *Chem. Mater.* **2010,** *22,* 70–76
DOI:10.1021/cm9021563

CHEMISTRY OF MATERIALS
Article

O-*K* and Co-*L* XANES Study on Oxygen Intercalation in Perovskite $SrCoO_{3-\delta}$

Lassi Karvonen,[†] Markus Valkeapää,[†] Ru-Shi Liu,[‡] Jin-Ming Chen,[§] Hisao Yamauchi,[†] and Maarit Karppinen*,[†]

[†]*Laboratory of Inorganic Chemistry, Department of Chemistry, Helsinki University of Technology, FI-02015 TKK, Finland,* [‡]*Department of Chemistry, National Taiwan University, Taipei 10617, Taiwan, ROC, and* [§]*National Synchrotron Radiation Research Center, Hsinchu 30076, Taiwan, ROC*

Received July 16, 2009. Revised Manuscript Received November 18, 2009

Evolution of the O-*K* and Co-*L* edge XANES spectra for $SrCoO_{3-\delta}$ upon increasing oxygen content from 2.50 to 2.82 reveals that superoxide (O_2^-) related features are overwhelmingly strong in the surface region of highly oxygen-deficient samples. Moreover, should it be always present in the bulk, octahedrally coordinated cobalt is unobservable in the surface region of highly oxygen-deficient samples. On the other hand, the surface region hosts square-pyramidally coordinated cobalt even in brownmillerite $SrCoO_{2.50}$. Observations in the present work support an oxygen-intercalation mechanism in which (i) O_2 is first absorbed on the surface as O_2^-, (ii) then reductively split into O^{x-} associated with square-pyramidally coordinated cobalt, and (iii) finally in the bulk eventually reoxidized to O^{z-} ($0 < z < x$) being attached to octahedrally coordinated cobalt. The fact that only minute chemical shifts of the Co-*L* edge branches are seen indicates that electron transfer mostly takes place between oxygen atoms.

Introduction

Topotactic oxygen intercalation through chemical or electrochemical oxidation has proven to be a successful method to produce new ordered structures out of many late 3*d* transition metal oxides. Such intercalation typically occurs at low temperatures and leaves the cation lattice intact (excluding minor distortions). In many cases, the new structure yielded is found to be destabilized already at moderate temperatures (100−300 °C). Two of the most well-known oxide systems being prone to topotactic oxidation are (i) the Ruddlesden−Popper oxides such as $La_2CoO_{4+\delta}$,[1] $La_2NiO_{4+\delta}$,[2] and $La_2CuO_{4+\delta}$,[3]; and (ii) the perovskite oxides such as $SrFeO_{3-\delta}$[4,5] and $SrCoO_{3-\delta}$,[6−10] the former accommodating the intercalated oxygen at interstitial sites and the latter at oxygen vacancy sites. Examples of other structure types to allow topotactic intercalation of oxygen are $YBaCo_4O_{7+\delta}$,[11] $YCuO_{2+\delta}$[12] and $YBa_2Cu_3O_{7-\delta}$.[13]

Previous results from topotactic electrochemical oxidation experiments[14−16] suggest that oxygen diffusion into the material has two stages: (i) fast diffusion occurring via a network of extended defects and (ii) slow diffusion inside microdomains enclosed by the defect network leading to observable structural changes. There have been various suggestions for the diffusing oxygen species, that is, O^{2-}, O_3^{5-}, O^-, O_2^{2-}, and O_2^-. Recent results imply that, while the oxygen species intercalated through interstitial positions, as e.g. in the case of the Ruddlesden−Popper oxides,[17,18] have more O^{2-} character, intercalation through vacancies, as is the case with the perovskite oxides,[8] rather involves O^--type species. Surface-sensitive techniques have also detected peroxide-like and even

*Author to whom correspondence should be addressed. Phone: +358-9-470-22600. Fax: +358-9-462373. E-mail: maarit.karppinen@tkk.fi.

(1) Nemudry, A.; Rudolf, P.; Schöllhorn, R. *Solid State Ionics* **1998**, *109*, 213.
(2) Bhavaraju, S.; DiCarlo, J. F.; Scarfe, D. P.; Jacobson, A. J.; Buttrey, D. J. *Solid State Ionics* **1996**, *86−88*, 825.
(3) Rudolf, P.; Schöllhorn, R. *J. Chem. Soc., Chem. Commun.* **1992**, 1158.
(4) Nemudry, A.; Weiss, M.; Gainutdinov, I.; Boldyrev, V.; Schöllhorn, R. *Chem. Mater.* **1998**, *10*, 2403.
(5) Tsujimoto, Y.; Tassel, C.; Hayashi, N.; Watanabe, T.; Kageyama, H.; Yoshimura, K.; Takano, M.; Ceretti, M.; Ritter, C.; Paulus, W. *Nature* **2007**, *450*, 1062.
(6) Bezdicka, P.; Wattiaux, A.; Grenier, J. C.; Pouchard, M.; Hagenmuller, P. *Z. Anorg. Allg. Chem.* **1993**, *619*, 7.
(7) Nemudry, A.; Rudolf, P.; Schöllhorn, R. *Chem. Mater.* **1996**, *8*, 2232.
(8) Le Toquin, R.; Paulus, W.; Cousson, A.; Prestipino, C.; Lamberti, C. *J. Am. Chem. Soc.* **2006**, *128*, 13161.
(9) Karvonen, L.; Räsänen, S.; Yamauchi, H.; Karppinen, M. *Chem. Lett.* **2007**, *36*, 1176.
(10) Karvonen, L.; Yamauchi, H.; Karppinen, M. *Chem. Mater.* **2008**, *20*, 7143.
(11) Räsänen, S.; Yamauchi, H.; Karppinen, M. *Chem. Lett.* **2008**, *37*, 638.
(12) Trari, M.; Töpfer, J.; Doumerc, J. P.; Pouchard, M.; Ammar, A.; Hagenmuller, P. *J. Solid State Chem.* **1994**, *111*, 104.
(13) Hinks, D. G.; Chmaissem, O.; Ely, L.; Scott, C.; Jorgensen, J. D.; Akujieze, J. K. *Physica C* **2000**, *333*, 1.
(14) Goldberg, E.; Nemudry, A.; Boldyrev, V.; Schöllhorn, R. *Solid State Ionics* **1998**, *110*, 223.
(15) Goldberg, E.; Nemudry, A.; Boldyrev, V.; Schöllhorn, R. *Solid State Ionics* **1999**, *122*, 17.
(16) Nemudry, A.; Goldberg, E. L.; Aguirre, M.; Alario-Franco, M. Á. *Solid State Sci.* **2002**, *4*, 677.
(17) Le Toquin, R.; Paulus, W.; Cousson, A.; Dhalenne, G.; Revcolevschi, A. *Physica B* **2004**, *350*, e269.
(18) Paulus, W.; Cousson, A.; Dhalenne, G.; Berthon, J.; Revcolevschi, A.; Hosoya, S.; Treutmann, W.; Heger, G.; Le Toquin, R. *Solid State Sci.* **2002**, *4*, 565.

 Published on Web 12/16/2009

superoxide-like species both in Ruddlesden−Popper and perovskite type oxides.[19−21]

The $SrCoO_{3-\delta}$ system has been known for its wide oxygen-deficiency range ($2.29 < 3-\delta < 3.00$) including oxygen-ordered phases of orthorhombic,[22,23] tetragonal,[22] and cubic[6−8] symmetries. Orthorhombic $SrCoO_{2.50}$ which consists of alternating layers of corner-sharing CoO_4 tetrahedra and CoO_6 octahedra (as in the case of the mineral brownmillerite) is the most oxygen-deficient phase still exhibiting an oxygen ordering.[23] Intercalation of oxygen into the $SrCoO_{2.50}$ ($n = 2$) phase turns it to the cubic $SrCoO_{3.00}$ ($n = \infty$) phase via a cascade of tetragonally distorted oxygen-ordered $SrCoO_{(3n-1)/n}$ phases with oxygen contents of $(3n-1)/n$ per formula unit. In addition to the earlier reported $n = 4$, 5, and 8 intermediate phases in electrochemically[7,8] and high-pressure and high-temperature[22] oxygenated samples, we recently observed the existence of the $n = 6$ and 7 phases in our multiphase samples of $SrCoO_{3-\delta}$ ($2.50 < (3-\delta)_{aver} < 2.87$) prepared through chemical oxygenation.[10] Availability of wide selection of oxygen-ordered intermediate structures, close to each other in the free energy, is a likely reason behind the low-temperature oxygen mobility in $SrCoO_{3-\delta}$.[8]

The purpose of this work is to study the oxygenation process in the $SrCoO_{3-\delta}$ system as seen through O-*K* and Co-*L* edge XANES (X-ray absorption near-edge structure) spectroscopy. Only few XANES studies have focused on the oxygen deficiency in perovskites.[8,19,24,25] Imamura et al.[19] specifically highlighted the possibilities of depth-resolved XANES spectroscopy for such oxygen-deficient materials. The present study on the $SrCoO_{3-\delta}$ system is an extension of their work. Here we observe that the features assigned to O_2^- superoxide in $(La_{1-x}Sr_x)$-$CoO_{3-\delta}$ ($x = 0.0$ - 0.2)[19] become much more prominent at the $x = 1.0$ end phase, that is, $SrCoO_{3-\delta}$. Combining surface-specific total-electron-yield (TEY) and bulk-emphasized fluorescence-yield (FY) data for the O-*K* edge we show that the preferences among different oxygen species and coordination spheres of cobalt significantly vary from the surface region to the interior of the material. The Co-*L* edge data are consistent with the conclusions made on the basis of O-*K* edge data.

Experimental Section

Sample Preparation. A series of seven samples with gradually varied oxygen contents was prepared through oxidizing powder specimens of $SrCoO_{2.5}$ precursor with Br_2. The precursor powder was prepared through an EDTA (ethylenediaminetetraacetic acid) method from stoichiometric amounts of Co and $SrCO_3$. Chunks of cobalt metal were first dissolved in hot concentrated HNO_3, to which $SrCO_3$ powder was then added after adjusting the HNO_3 concentration to 3 M. The metal nitrate solution was poured into an equal volume of concentrated ammonia solution containing EDTA in 50% excess against the total amount of metal ions. The solution was heated to dryness, the residual being burned and then calcined in air at 900 °C for 5 h. Finally, the calcined powder was pelletized and sintered in air at 1100 °C for 60 h, followed by quenching to room temperature. The product was confirmed to be of an XRD-pure sample of the orthorhombic brownmillerite phase. The oxygen content was determined by iodometric titration to be 2.50 per formula unit.

In the present Br_2 oxygenation technique[10] the precursor powder is immersed into Br_2/CH_3CN solution and the degree of oxygenation is adjusted by controlling the immersion time and temperature as well as the Br_2 and H_2O contents. The primary oxygen source in this process appears to be H_2O, which is either absorbed from the surrounding atmosphere by the hygroscopic solvent or is deliberately added. Immersions were carried out by adding 2.5 mL of 2.5 M Br_2/CH_3CN over 200 mg of dry precursor powder in 8.5 × 2.5 cm test tubes. The tubes were covered with a clock glass and placed in a bath filled with 25 °C water. Part of the immersions included 0.6 M of added H_2O in order to speed up the oxygenation. The experimental parameters, that is, immersion time and H_2O concentration, for the oxygenation treatments are given in Table 1.

Oxygen-Content Analysis. The average oxygen content per formula unit, $(3-\delta)_{aver}$, was determined for each sample using iodometric titration: ~20 mg of sample powder was dry-mixed with excess of KI and dissolved under N_2 atmosphere in 30 mL of 1 M HCl solution made oxygen-free by continuous N_2 bubbling. Oxidation of KI by Co^{III} and/or Co^{IV} liberates iodine in a stoichiometric relation that is dependent on the average formal cobalt valence and thereby on the oxygen content of the sample. The amount of iodine was determined by titrating with 0.015 M $Na_2S_2O_8$ solution immediately after its generation. The indicator used for detecting the titration end-point was 1 mL of saturated starch solution, added right before the end-point was reached. Titration was repeated two or three times for each sample with reproducibility better than ±0.01 for the average oxygen content, $(3-\delta)_{aver}$.

XRD Experiments. X-ray powder diffraction (XRD) patterns were recorded for the $SrCoO_{3-\delta}$ samples using Cu-K_α radiation (Philips MPD 1880). Patterns were analyzed through multiphase Le Bail matching using the software FULLPROF[26] in order to acquire data on phase fractions of the various $SrCoO_{(3n-1)/n}$ phases.[10] The profile of the remaining brownmillerite phase in the oxygenated samples was matched using the orthorhombic space group *Imma* and lattice parameters, $a = 5.4683$ Å, $b = 15.7526$ Å, and $c = 5.5704$ Å, which had been determined for the single-phase precursor powder of $SrCoO_{2.50}$.[10] In addition to the phase information of the brownmillerite precursor, our input file contained up to five $SrCoO_{(3n-1)/n}$ phases with cubic (*Pm*-3*m*) unit cells and lattice parameters determined in our previous work.[10] Pattern matching was made such that phases apparently not existing in the sample were excluded from the profile fitting. It should be noted that cubic

(19) Imamura, M.; Matsubayashi, N.; Shimada, H. *J. Phys. Chem. B* **2000**, *104*, 7348.
(20) Rogers, J. W., Jr; Shinn, N. D.; Schirber, J. E.; Venturini, E. L.; Ginley, D. S.; Morosin, B. *Phys. Rev. B* **1988**, *38*, 5021.
(21) Zhou, J.; Sinha, S.; Goodenough, J. B. *Phys. Rev. B* **1989**, *39*, 12331.
(22) Takeda, Y.; Kanno, R.; Takada, T.; Yamamoto, O.; Takano, M.; Bando, Y. *Z. Anorg. Allg. Chem.* **1986**, *540*/*541*, 259.
(23) Grenier, J. C.; Ghodbane, S.; Demazeau, G.; Pouchard, M.; Hagenmuller, P. *Mater. Res. Bull.* **1979**, *14*, 831.
(24) Moodenbaugh, A. R.; Nielsen, B.; Sambasivan, S.; Fischer, D. A.; Friessnegg, T.; Aggarwal, S.; Ramesh, R.; Pfeffer, R. L. *Phys. Rev. B* **2000**, *61*, 5666.
(25) Horiba, K.; Eguchi, R.; Taguchi, M.; Chainani, A.; Kikkawa, A.; Senba, Y.; Ohashi, H.; Shin, S. *Phys. Rev. B* **2007**, *76*, 155104.
(26) Rodriguez-Carvajal, J. Abstracts of the Satellite Meeting on Powder Diffraction of the XV Congress of the IUCr, **1990**; p 127.

Table 1. Experimental Parameters Used in the Oxygenation Treatment, Phase Fractions of the Detected $n = 2, 4, 5, 6$ Homologues (As Determined from Le Bail Profile Matching) and Average Oxygen Contents per $SrCoO_{3-\delta}$ Formula Unit of the Present Samples

			phase fractions				
sample name	oxygenation parameters	$(3-\delta)_{iodo}$[a]	$n = 2$	$n = 4$	$n = 5$	$n = 6$	$(3-\delta)_{xrd}$[b]
2.50(P)		2.50(1)	1.00				2.50(5)
2.53(D)	2 h, 25 °C	2.53(1)	0.731(5)	0.237(5)	0.032(5)		2.57(5)
2.56(D)	3 h, 25 °C	2.56(1)	0.363(5)	0.169(5)	0.468(5)		2.68(5)
2.63(D)	4 h, 25 °C	2.63(1)	0.299(5)	0.306(5)	0.395(5)		2.69(5)
2.63(H)	1 h, 25 °C, 0.6 M H_2O	2.63(1)	0.356(5)	0.644(5)			2.66(5)
2.70(H)	3 h, 25 °C, 0.6 M H_2O	2.70(1)	0.154(5)	0.733(5)	0.113(5)		2.72(5)
2.76(H)	5 h, 25 °C, 0.6 M H_2O	2.76(1)	0.031(5)	0.259(5)	0.613(5)	0.097(5)	2.78(5)
2.82(H)	9 h, 25 °C, 0.6 M H_2O	2.82(1)		0.026(5)	0.131(5)	0.844(5)	2.83(5)

[a] $(3-\delta)_{iodo}$ = average oxygen content determined through iodometry. [b] $(3-\delta)_{xrd}$ = average oxygen content estimated using the sum of the ideal oxygen contents of the $SrCoO_{(3n-1)/n}$ homologues weighted by their phase fractions.

unit cells were used, since the splits and extra reflections due to the tetragonal superlattices were so weak that using *Pm*-3*m* covered the oxygenated phase profile well enough for the present purpose.

XANES Experiments. XANES spectra were collected at the BL20A high-energy spherical grating monochromator (HSGM) beamline of Taiwan's National Synchrotron Radiation Research Center (NSRRC). The X-ray photons were monochromatized with horizontal and vertical focusing mirrors, a spherical grating monochromator with four gratings and one toroidal refocusing mirror. The incident photon flux (I_0) exiting the monochromator was monitored by Ni mesh placed on the beamline after the monochromator exit slit. The O-*K* XANES spectra were recorded in single scan for each sample simultaneously in FY and TEY modes, while the detection of Co-*L* XANES spectra was made only in TEY mode. Probing depths of FY (1000−2000 Å) and TEY (20−50 Å) modes are different,[27] the latter giving more surface-region-specific information. In the FY mode a microchannel-plate (MCP) detector system with an electrically isolated grid mounted in front was employed. The grid was set to 50 V, the front of the MCPs to −3200 V and the rear to −200 V. The grid bias ensures that positive ions do not enter the detector, while the MCP bias ensures that no electrons are detected. The detector was located normal to the sample, and photons were incident at an angle of 45° with respect to the sample normal. In the TEY mode, the signal recorded is the sample drain current. Measurements were done at room temperature in vacuum for samples of powder form. In order to conserve the differences between the surface and bulk, no additional crushing or grinding was made prior to the measurements. Energy resolution of the monochromator was ∼0.22 eV. The photon energies were calibrated with accuracy better than 0.1 eV using the known O *K*-edge and Co *L*-edge absorption peaks of CuO and CoO references. The FY and TEY signals were normalized in terms of simultaneously measured I_0 signal. Raw spectral data sets gained this way were processed through different procedures, depending on the detection mode and the absorption edge.

Pre-edge background subtraction and postedge normalization to unity for O-*K* edge spectra were performed by using average intensities of three subsequent data points closest to 523 and 610 eV for pre- and postedge region, respectively. An additional self-absorption correction (SAC) for the FY data was done using a software named ATHENA.[28] The noise in the single-scan FY data was dealt with a simple smoothing procedure (see the Supporting Information (SI)). From the smoothed spectra, the energy positions of the selected peaks were determined through finding the corresponding local minima of the second derivatives of the spectra.

The Co-*L* edge spectra were normalized as follows. First the pre-edge was subtracted by using the average intensity of three points closest to 772 eV as zero level. A straight-line for modeling the linear characteristics of the rising-edge background was then fitted to the spectra. Data points used for the fit were three subsequent points closest to 790 eV plus three subsequent points closest to 806 eV. Finally the spectral intensities were divided by a scaling factor defined as the intensity of the fitted line at 806 eV. The shift of each branch in terms of the oxygen content,[29−32] was monitored through observing the branch's center of gravity position. Positive shift implies an increment in actual valence at the absorber site. The spectral regions engaged with the L_3 and L_2 branches were defined as 772−790 eV and 790−806 eV, respectively. The branching ratio as defined by $L_3/(L_3 + L_2)$ was also calculated. Theoretical model calculations have predicted that an increase in the branching ratio indicates an increase in the spin state of the absorber.[33] Hu et al.[29] demonstrated that the theoretically predicted change exceeded the practical limit of detection in the case of compounds with $3d^4$ to $3d^6$ electron configurations.

Results and Discussion

Chemical and Crystal-Chemical Characteristics. The average oxygen contents, $(3-\delta)_{aver}$, of our samples ranged from 2.50 to 2.82 according to iodometric determination. XRD data revealed that three oxygenated $SrCoO_{(3n-1)/n}$ homologues with $n = 4$, 5, and 6, were present in the samples besides the original $n = 2$ precursor phase, gradually disappearing with increasing $(3-\delta)_{aver}$. Pseudocubic lattice parameters, $a_{(n=4)} = 3.84670$ Å, $a_{(n=5)} = 3.84176$ Å and $a_{(n=6)} = 3.83786$ Å,[10] were employed in determining the fractions of the oxygenated phases in each sample, see Table 1. The ideal oxygen contents of the

(27) (a) Nakajima, R.; Stöhr, J.; Idzerda, Y. U. *Phys. Rev. B* **1999**, *59*, 6421. (b) Koningsberger D. C., Prins, R., *X-ray Absorption: Principles, Application, Techniques of EXAFS, SEXAFS and XANES*; John Wiley & Sons: New York, 1988.
(28) Ravel, B.; Newville, M. *J. Synchrotron Radiat.* **2005**, *12*, 537.
(29) Hu, Z.; Grazioli, C.; Knupfer, M.; Golden, M. S.; Fink, J.; Mahadevan, P.; Kumar, A.; Ray, S.; Sarma, D. D.; Warda, S. A.; Reinen, D.; Kawasaki, S.; Takano, M.; Schüssler-Langeheine, C.; Mazumdar, C.; Kaindl, G. *J. Alloys Compd.* **2002**, *343*, 5.
(30) Yoon, W. S.; Kim, K. B.; Kim, M. G.; Lee, M. K.; Shin, H. J.; Lee, J. M.; Lee, J. S.; Yo, C. H. *J. Phys. Chem. B* **2002**, *106*, 2526.
(31) Hu, Z.; Kaindl, G.; Warda, S. A.; Reinen, D.; de Groot, F. M. F.; Müller, B. G. *Chem. Phys.* **1998**, *232*, 63.
(32) Hu, Z.; Golden, M. S.; Fink, J.; Kaindl, G.; Warda, S. A.; Reinen, D.; Mahadevan, P.; Sarma, D. D. *Phys. Rev. B* **2000**, *61*, 3739.
(33) Thole, B. T.; van der Laan, G. *Phys. Rev. B* **1988**, *38*, 3158.

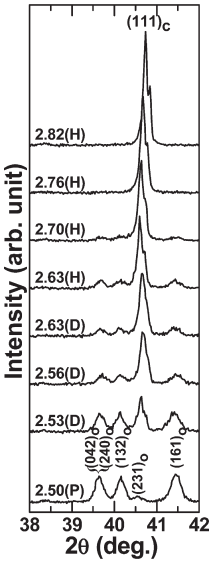

Figure 1. Progress in the oxygenation of $SrCoO_{2.50}$ demonstrated through the enhancement of the pseudocubic $(111)_c$ XRD reflection of the $SrCoO_{3-\delta}$ ($3-\delta > 2.50$) phase with the expense of the orthorhombic $(042)_o$, $(240)_o$, $(132)_o$, $(231)_o$ and $(161)_o$ reflections of the $SrCoO_{2.50}$ phase.

four $SrCoO_{(3n-1)/n}$ homologues were used together with their XRD phase fractions in order to calculate estimates for $(3-\delta)_{aver}$, that is, $(3-\delta)_{xrd}$ in Table 1. Good agreements with the iodometrically determined values, that is, $(3-\delta)_{iodo}$ in Table 1, were confirmed. Pseudocubic $(111)_c$ diffraction peaks shown in Figure 1 indicate the degree of sample quality. Peaks for the samples oxygenated without H_2O addition tend to be more rounded. This may indicate that the single-crystal domains are smaller in the samples oxygenated without H_2O addition than in those oxygenated with added H_2O. Moreover, as seen from the phase fraction data (Table 1), H_2O addition favors the formation of a certain phase at a time which also sharpens the peak shape. In the following discussion of XANES data, samples are referred to according to the names given in Table 1, indicating the $(3-\delta)_{iodo}$ value and the sample preparation history (P = precursor, D = oxygenated without added H_2O and H = oxygenated with added H_2O).

Several kinds of cobalt coordination environment coexist in $SrCoO_{3-\delta}$ over the oxygenation range studied. Tetrahedral coordination is expected so long as the pristine orthorhombic $SrCoO_{2.50}$ phase remains in the sample. In the course of oxygen-intercalation, the tetrahedral coordination is first replaced by an intermediate coordination, most probably square-pyramidal, which will later be complemented into octahedral coordination. Octahedral coordination is present in all the phases, the fraction of it monotonically increasing with increasing oxygen content. Except for the phases $SrCoO_{2.50}$ (50% octahedral and 50% tetrahedral), $SrCoO_{2.875}$ (75% octahedral and 25% square-pyramidal) and $SrCoO_3$ (100% octahedral),[8,23] no conclusive structure data have been reported to answer the question on oxygen ordering or coordination in different phases in the $SrCoO_{3-\delta}$ system.

O-*K* Edge XANES Analysis. In Figure 2, evolution of the O-*K* XANES spectrum with increasing $(3-\delta)_{aver}$ is

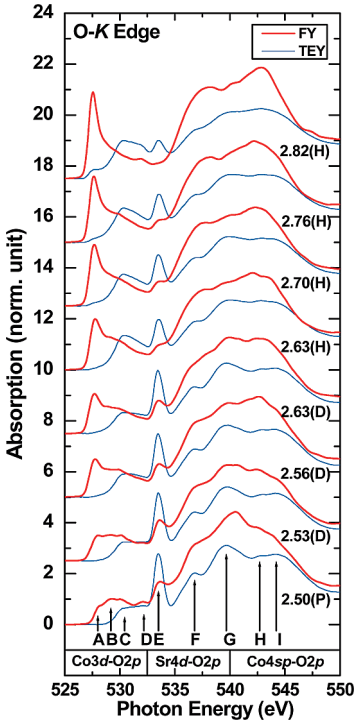

Figure 2. Evolution of the O-*K* edge XANES with $(3-\delta)_{aver}$. See Table 2 for assignment of features A-I. For clarity, the patterns are vertically shifted from each other.

Table 2. Main Character of the Hole States Delivering the Main Features at the O-*K* Edge

feature	hole state
A	Co3d_{xy}, Co3d_{xz} (octahedral coordination) + O2p ligand hole
B	Co3d_{yz}, Co3$d_{x^2-y^2}$ (octahedral coordination)
C	Co3d (square-pyramidal coordination)
D	Co3$d_{3z^2-r^2}$ (octahedral coordination)
E	σ^* resonance of O_2^- species
F	Sr4d
G	Co4sp (hybridization with O_2^- species)
H	Co4sp (hybridization with monoxidic species)
I	Co4sp (hybridization with monoxidic species)

shown. The pre-edge features in the O-*K* XANES spectra originate from transitions of electrons from the O1s core-state to hole-states of p character. In transition metal oxides, the target states are typically mixed states due to the hybridization of O2p ligand-hole state with s, p, and d states of the neighboring atoms. The visibility of a state depends on the availability of O2p ligand-hole states, working as dipole-allowed excitation channels, and their hybridization with the mixing orbital. Completely ionic oxides therefore cannot exhibit O-*K* pre-edge structures. There are, in total, nine features, heaps, or shoulders, observable in the pre-edge region for the present samples. These are indicated with letters A to I in Figure 2, and categorized into three areas of different hybrid structures[34] as follows: A−D: Co3d-O2p, E−G: Sr4d-O2p, and H−I: Co4sp-O2p. Observing the evolution of spectra in terms of oxygen content we recognize that features A, E, and G show significant changes. Feature A drifts down

(34) Wu, Z. Y.; Benfatto, M.; Pedio, M.; Cimino, R.; Mobilio, S.; Barman, S. R.; Maiti, K.; Sarma, D. D. *Phys. Rev. B* **1997**, *56*, 2228.

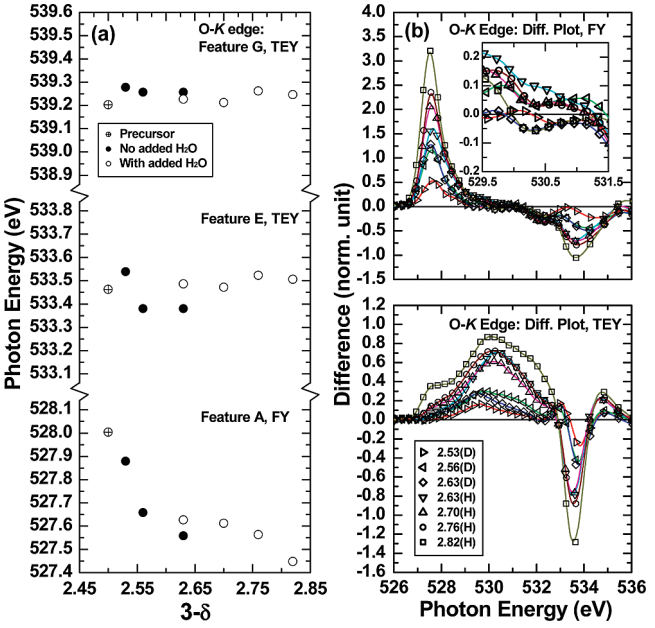

Figure 3. (a) Energy positions of the O-*K* edge XANES features A, E, and G as a function of $(3\text{-}\delta)_{aver}$ and oxidizing medium. (b) Difference plots illustrating the changes of the feature A−E intensities with $(3\text{-}\delta)_{aver}$ as compared to the sample 2.50(P) (FY data: upper panel, TEY data: lower panel). Inset: magnification of the FY-plots in the region 529.5−531.5 eV comprising the pyramidal feature C.

toward lower photon energies (see Figure 3(a)) and gains intensity as oxygen content increases (see Figure 3(b)), being in agreement with the scheme for ligand-hole feature of negative-charge-transfer compounds.[35] Note that many oxides of late first row transition metals with high formal oxidation numbers ($Mn^{III/IV}$, $Fe^{III/IV}$, $Co^{III/IV}$, $Ni^{II/III}$, $Cu^{II/III}$) are known to have significant covalent character in their bonding,[35−38] and accordingly partial charge of oxygen anions may well deviate from the formal-II oxidation number toward null, stabilizing the O2*p* ligand-hole state as the lowest unoccupied orbital.[39] In this case an intensive feature originating from the $3d^{n+l}\boldsymbol{L}_l \rightarrow \boldsymbol{c}3d^{n+l}\boldsymbol{L}_{l-1}$ ($\boldsymbol{L}$ = oxygen ligand hole, $\boldsymbol{c}$ = oxygen core hole) transition stands out at the O-*K* pre-edge threshold, beside the features originating from the $3d^{n+l}\text{-}\boldsymbol{L}_l \rightarrow \boldsymbol{c}3d^{n+l+1}\boldsymbol{L}_l$ transition. Since intensity of feature A follows the same trend as that for the expected population of octahedrally coordinated cobalt, the ligand hole is likely specific for octahedral coordination. Linking the feature A with the octahedral coordination is also supported by the recent band-structure calculations for the $SrCoO_{2.50}$ brownmillerite structure by Pardo et al.[40] using LDA+*U* approximation. The calculated partial density of states (DOS) of Co3*d* split by distorted octahedral crystal field fits well with the profile of the Co3*d*-O2*p* hybrid structure recorded from our $SrCoO_{2.50}$ precursor. Similar narrow low-energy structure as feature A ($Co3d_{xz}$ and $Co3d_{xy}$) can be observed. In the theoretical results feature A holds a strong Co3*d* character unlike stated by us above. However, the overall calculated DOS below the Fermi level presents a dominant O2*p* character indicating that our ligand-hole assignment for feature A becomes quickly more reasonable with increasing oxygen content. Feature A is prominent in the FY data, whereas in TEY data it is visible only for the oxygen richest samples, 2.70(H), 2.76(H), and 2.82(H). This indicates that the octahedral coordination is promoted in the bulk and suppressed at the surface.

The intensities of both features E and G follow a trend opposite to that of feature A. They get weaker with increasing oxygen content while the energy positions remain fixed at 533.5 eV for E and at 539.2 eV for G in TEY (see Figure 3(a)). Feature E stands out from the rest of the Sr4*d*-O2*p* hybrid structure region with its narrow line width, indicating that it may not originate from the Sr4*d*-O2*p* hybridization. Imamura et al.[19] combined simultaneously recorded partial electron yield (PEY), TEY, and FY O-*K* XANES data for depth-specific analysis of the oxygen-deficient $(La_{0.8}Sr_{0.2})CoO_{3-\delta}$ system. They confirmed a superoxide species O_2^- to exist particularly in the surface region of this material. Ruckman et al.[41] studied O_2^- species in Li, K and Cs matrices deposited on Ar surface at 20 K to conclude that O_2^- delivers two intensive features at about 529.0 and 534.5 eV, respectively arising from a π^* resonance due to $O1s \rightarrow O1\pi_g$(antibonding) transition and a σ^* resonance due to $O1s \rightarrow O3\sigma_u$(antibonding) transition. When the electron population is increased in the lowest unoccupied orbital, that is, antibonding $1\pi_g$ (that is, when the O_2^- species is reduced toward peroxide O_2^{2-} and weaker bond strength), the π^* and σ^* resonances move toward lower energies. The red-shifted feature E (533.5 eV) lies in the range of energy variation expected for the σ^* resonance originating from O_2^-. Feature G may be recognized as an O_2^- component of the Co4*sp*-O2*p* hybrid, in line with conclusions by Ruckman et al.[41] In superoxides, O_2^- components of the Co3*d*-O2*p* hybrid are also expected to mask the π^* resonance which therefore is not observable in our data. Another reason for the π^* resonance extinction may be that the said O_2^--related species has already been strongly reduced toward peroxide which should have an extinguishing effect on the π^* resonance line. This situation seems parallel to the red shift of σ^* resonance as compared with those observed in alkaline superoxides.

Final assignments of features A−I are summarized in Table 2. We assume the feature B also to represent the Co3*d* orbitals of octahedrally coordinated cobalt, since the intensity change with oxygen content (and between

(35) Abbate, M.; Zampieri, G.; Okamoto, J.; Fujimori, A.; Kawasaki, S.; Takano, M. *Phys. Rev. B* **2002**, *65*, 165120.
(36) Saitoh, T.; Bocquet, A. E.; Mizokawa, T.; Namatame, H.; Fujimori, A.; Abbate, M.; Takeda, Y.; Takano, M. *Phys. Rev. B* **1995**, *51*, 13942.
(37) Sarma, D. D.; Rader, O.; Kachel, T.; Chainani, A.; Mathew, M.; Holldack, K.; Gudat, W.; Eberhardt, W. *Phys. Rev. B* **1994**, *49*, 14238.
(38) Sarma, D. D.; Strebel, O.; Simmons, C. T.; Neukirch, U.; Kaindl, G.; Hoppe, R.; Müller, H. P. *Phys. Rev. B* **1988**, 37 9784.
(39) Kuiper, P.; Kruizinga, G.; Ghijsen, J.; Sawatzky, G. A.; Verweij, H. *Phys. Rev. Lett.* **1989**, *62*, 221.
(40) Pardo, V.; Botta, P. M.; Baldomir, D.; Rivas, J.; Piñeiro, A.; de la Calle, C.; Alonso, J. A.; Arias, J. E. *Physica B* **2008**, *403*, 1636.
(41) Ruckman, M. W.; Chen, J.; Qiu, S. L.; Kuiper, P.; Strongin, M.; Dunlap, B. I. *Phys. Rev. Lett.* **1991**, *67*, 2533.

TEY and FY data) is parallel to the case of the octahedral ligand-hole feature A. The partial DOS of Co3*d* split by distorted octahedral crystal field in $SrCoO_{2.50}$ calculated by Pardo et al.[40] also showed a broad structure in this region (Co3d_{yz} and Co3$d_{x^2-y^2}$). Following the same reference,[40] the feature D, as well, is understood mainly as originating from Co3*d* in octahedral coordination (Co3$d_{3z^2-r^2}$). This appears reasonable, when TEY data is observed at the highest oxygen content: Clear intensification of the feature D follows the appearance of the other octahedral features. Feature C, although enhanced in TEY data, remains well visible even in FY, indicating that the coordination behind this feature should be present in both the surface region and the bulk. Referring again to the work by Pardo et al.[40] this region should contain the partial DOS of Co3*d* split in tetrahedral crystal field. However, in the FY data the region of the feature C (peaked at about 530.5 eV in TEY) exhibits a slight increase in intensity in the course of oxygenation at low-oxygen contents (see the inset of Figure 3(b)), while the intensity drops at high oxygen contents. This kind of behavior refers to some intermediate coordination rather than a tetrahedral coordination, the fraction of which is expected to decline monotonously in the course of oxygenation. In the TEY data, together with the absence of octahedral features, the overall intensification of the region of the feature C with increasing oxygen content indicates the preference of surface-region cobalt having this coordination over the whole oxygen-content range studied including the lower end. Furthermore, since this is coupled with the decrease of O_2^--related features E and G, feature C cannot be related to O_2^- but must be originated from the oxygen coordinating to cobalt as monoxidic species. We then regard feature C as arising from the square-pyramidal coordination, present in the whole structure but favored in the surface region at an expense of octahedral coordination.

The reason why tetrahedral coordination seems not to produce features strong enough to be observed in our data might result from the weak hybridization as compared to the octahedral and square-pyramidal coordinations. This comes out from the reasoning that in $SrCoO_{2.50}$ the number of oxygen atoms seeing only octahedrally coordinated cobalt in the octahedral layer is twice as much as that seeing only tetrahedrally coordinated cobalt in the tetrahedral layer. In addition to the smaller coordination number, this is also caused by no directly opposite lobes between any of available O2*p* and Co3*d* orbitals in the tetrahedral coordination (whereas in octahedral/square-pyramidal coordination this occurs from six/five directions). For the same reason, the Co3*d*-O2*p* hybridization of oxygen atoms between the layers is considered to favor octahedrally coordinated cobalt.

Our O-*K* edge spectra may be viewed as a series of time-resolved still pictures of the oxygen intercalation process. (i) Intercalation starts with absorption of O_2 at the surface vacancies where the neutral molecule gets reduced toward O_2^- to yield the superoxide-related features E and G (that get enhanced in TEY). (ii) The excess electron population in the O1π_g (antibonding) orbital eventually splits the absorbed O_2 into O^{x-} anions that coordinate to the neighboring cobalt cations turning their coordination to square-pyramidal. This is manifested by the opposite oxygen-content dependency of the square-pyramidal C feature as compared to the superoxidic features E and G. We further consider that it is the vacancies neighboring the tetrahedrally coordinated cobalt which are favored as the O_2 absorption sites. (iii) Finally, deep in the bulk square-pyramidal coordination turns to octahedral one. This involves a reoxidation of O^{x-} to O^{z-} ($0 < z < x$) generating an intensive O2*p* ligand-hole feature A. Among steps i−iii the later step becomes more favored deep in the bulk. This view agrees with the trend of local oxygen concentration about the cobalt, being small in the surface region and increasing to a constant bulk value. The higher the local oxygen concentration, the higher the coordination number. Complementary oxygen is always taken from neighboring square-pyramidally coordinated cobalt atom which is closer to the surface than the receiving cobalt atom. Eventually, this rereleases the surface vacancies to be ready to absorb new O_2 molecules.

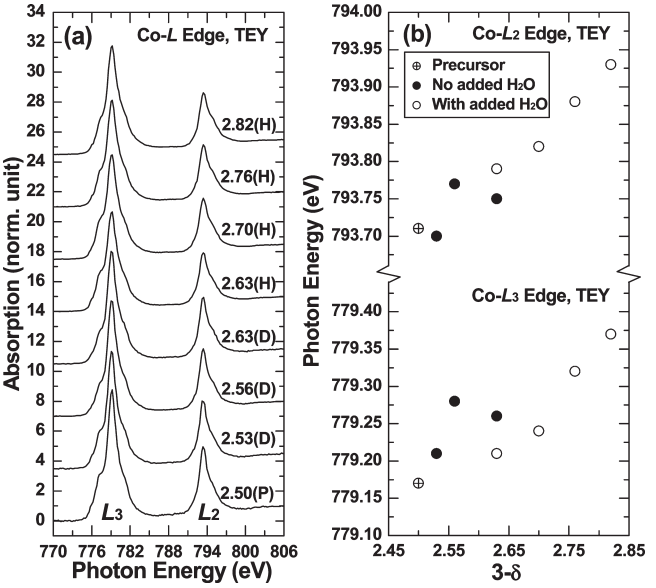

Figure 4. (a) Evolution of the Co-$L_{2,3}$ XANES edges and (b) the energy positions of the Co-L_2 and Co-L_3 centers of gravities as a function of $(3\text{-}\delta)_{aver}$ and oxidizing medium.

Co-*L* Edge XANES Analysis. The Co-$L_{2,3}$ XANES spectra are presented in Figure 4(a). The main peaks or the so-called white lines have shoulders on both the high- and low-energy sides. The more intensive shoulder is on the low-energy side for the L_3-edge (Co2$p_{3/2}$ → Co3*d* transition), whereas for the L_2-edge (Co2$p_{1/2}$ → Co3*d* transition) it is on the high-energy side. Only slightly more pronounced L_2-edge high-energy shoulder accompanied by weakened L_3-edge low-energy shoulder can be observed in the course of oxygenation. The spectra were compared with the calculated ones.[42] For our comparison

(42) van der Laan, G.; Kirkman, I. W. *J. Phys.: Condens. Matter* **1992**, *4*, 4189.

we have used the calculated L-edges of Co3d^6 in both octahedral and tetrahedral crystal fields. Additionally, in order to cover the cobalt with valence > 3, the calculated L-edge of Fe3d^5 in an octahedral crystal field was also taken into account. The latter choice is justified by the fact, that the shapes of the first-row transition metal L-edges in a specific crystal field are dependent mainly on the number of the d electrons of the absorbing element.[43] The strength of the octahedral crystal field in $SrCoO_{3-\delta}$ has been estimated to the 1−2 eV range.[44,45] In that case, the tetrahedral values should exist in the 0.5−1 eV range. According to the calculated spectra, the transfer from tetrahedrally to octahedrally coordinated Co3d^6 makes the low-energy side of Co-L_3 white line less pronounced. Also increasing the valence has similar effect on Co-L_3 coupled with more pronounced high-energy side of Co-L_2.

The values determined for the $L_3/(L_3 + L_2)$ branching ratio in our spectra lie between 0.69 and 0.71. When typical high- and low-spin branching ratios are ∼0.7 and ∼0.6, respectively,[29,33] this indicates that within the present oxygen-content range, cobalt essentially sustains the high-spin state.[23]

The shift of center of gravity is illustrated for the L_3 and L_2 branches in Figure 4(b). The observable +0.2 eV chemical shifts against the transfer of 0.64 e^- upon oxygenation ($\Delta\delta = -0.32$) is small compared to that observed for the $(La_{1-x}Sr_x)CoO_3$ system in which oxidizing transfer of 1 e^- ($\Delta x = 1$) results in a shift of +1 eV.[29] Hence the change in actual valence of cobalt in $SrCoO_{3-\delta}$ upon oxygenation must be quite small. Apparently the major part of electron transfer during oxygen intercalation takes place between different oxygen species and new hole-states created by oxygenation are accommodated as oxygen ligand holes (consistent with our interpretation of the O-K edge data given above). While our Co-$L_{2,3}$ TEY data cover only the surface region, an earlier study by Le Toquin et al.[8] on the Co-K edge (using transmission mode) gives bulk-emphasized information. They revealed that the electron transfer has $Co^{III} \rightarrow Co^{IV} + e^-$ character in the oxygen-content range of 2.50 to 2.725 and $O^{2-} \rightarrow O^-$ character in the range of 2.725−2.875. This further supports the present interpretation of the O-K and Co-$L_{2,3}$ edge data.

Conclusion

A series of samples of the $SrCoO_{3-\delta}$ system with average oxygen content $(3-\delta)_{aver}$ of 2.50−2.82 was thoroughly investigated for the depth-resolved O-K and Co-L edge XANES spectral features. The samples were prepared through chemical oxygenation of orthorhombic $SrCoO_{2.50}$ precursor using $Br_2/H_2O/CH_3CN$ as the oxidizing media.

The O-K XANES study revealed a significant absorption of O_2 as O_2^- species in the surface region. Difference in the Co−O coordination type in between the surface region and the bulk was clearly detected: the oxygen-rich bulk holds octahedral coordination, whereas the oxygen-poor surface region favors square-pyramidal and tetrahedral coordinations. Based on the O-K XANES results, we proposed an intercalation mechanism in which (i) oxygen intercalation starts from absorption of an O_2 molecule to fill an oxygen vacancy next to the tetrahedrally coordinated cobalt as an O_2^- superoxide species, (ii) then the O_2^- species is gradually reduced and split into an O^{x-} intermediate species to turn the neighboring Co−O coordination polyhedron from a tetrahedron to a square-pyramid, and (iii) finally, in the bulk the O^{x-} species is reoxidized to O^{z-} ($0 < z < x$) with a notable O2p ligand hole character. The fact that only very small chemical shifts of Co-$L_{2,3}$ edge were seen upon oxygenation was considered to support the idea that the intercalation processes mostly involve electron transfers between the oxygen atoms.

Acknowledgment. The present work was supported by Academy of Finland (Nos. 110433 and 126528), Tekes (No. 1726/31/07) and Emil Aaltonen Foundation.

Supporting Information Available: Smoothing procedure for O-K XANES FY spectra. This material is available free of charge via the Internet at http://pubs.acs.org.

(43) de Groot, F. M. F.; Fuggle, J. C.; Thole, B. T.; Sawatzky, G. A. *Phys. Rev. B* **1990**, *42*, 5459.
(44) Zhuang, M.; Zhang, W.; Hu, A.; Ming, N. *Phys. Rev. B* **1998**, *57*, 13655.
(45) Potze, R. H.; Sawatzky, G. A.; Abbate, M. *Phys. Rev. B* **1995**, *51*, 11501.